Supporting Information

Low-Field Dynamic Magnetic Separation by Self-Fabricated Magnetic Meshes for Efficient Heavy Metal Removal

Xiangxia Wei[†], Pon Janani Sugumaran[†], Erwin Peng, Xiao Li Liu[‡], and Jun Ding*

Department of Materials Science and Engineering, National University of Singapore, 117575, Singapore

Email: msedingj@nus.edu.sg

Present Address:

[‡]National Center for Nanoscience and Technology (NCNST), 100190 Beijing, P. R. China (X.L.L)

Fabrication of the magnetic filter by 3D printing

The magnetic filter with different layers in the main text was printed by a simple and cheap three-dimensional printer (3Dison Multi printer equipped with a ROKIT. Inc. extruder). The feedstock paste was loaded in a 10 mL plastic syringe, and the printing was driven by the rotating belt. The fabrication process consists of the paste preparation and post-processing. Additionally, the formulation of the as-prepared homogeneous paste for printing is summarized in Table S1.

Moreover, rheological properties of the aqueous pastes were shown in Figure S1a. Obviously, the apparent viscosity decreases linearly with shear rate on a logarithmic scale, exhibiting a shear-thinning behavior which facilitates the formation of a smooth filament. Additionally, thermogravimetric study was performed by heating up to 800 ^{o}C as illustrated in Figure S1b. The weight loss is attributed to the water evaporation and organic removal, including plasticizer PEG-400, binder PVA, and a small amount of dispersant.

Table S1 The paste composition of magnetic filter for extrusion-based 3D printing.

	NiO	ZnO	α-Fe_2O_3	Binder Solution[a]
Weight (g)	2.46	1.78	8.76	5.0 g (~6 mL)

[a]The binder solution is PVA aqueous solution (12.5 wt%) with a small amount of PEG-400 as plasticizer and Solsperse 20000 as dispersant.

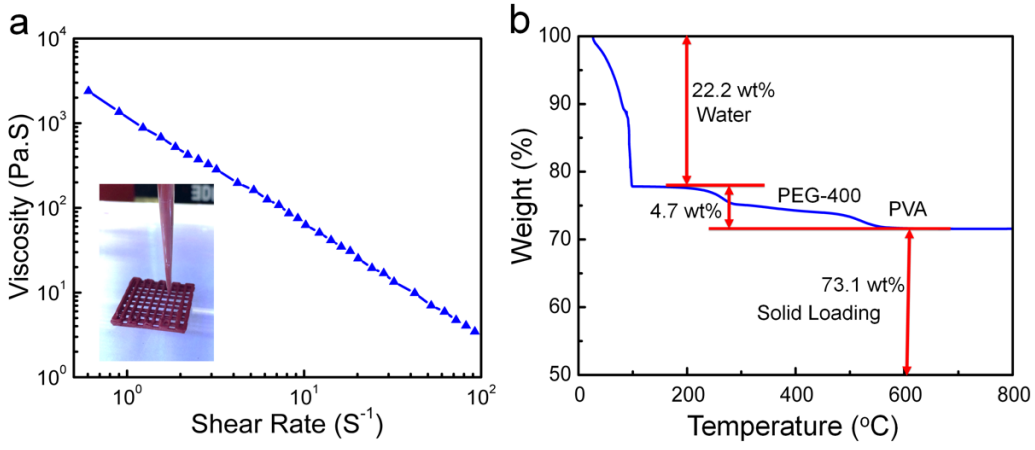

Figure S1 (a) Apparent viscosity as a function of shear rate of the printable paste. The inset shows the as-printed mesh. (b) TGA results of the paste heated at a ramp of 10 ^{o}C min^{-1}.

EDX analysis of the magnetic filter

To verify the composition of printed magnetic filter after heat treatment, EDX analysis was performed and confirmed the presence of Ni, Zn, Fe, and O. In the quantitative analyses the oxygen was omitted, and the composition of Ni, Zn, and Fe showed close similarity to the stoichiometric value calculated from the feed weight (Table S2).

Table S2 The element composition of magnetic filter after heat treatment.

Atomic composition (%)	Ni	Zn	Fe
Measured value	22.3	12.7	65.0
Stoichiometric value[a]	20.0	13.3	66.7

[a]Calculated from the weight ratio of the feed precursor powder.

XPS analysis of the magnetic filter

The XPS spectrum (Figure S2) on the printed filter after sintering indicated the presence of four elements peaks on the surface: Zn 2p, Ni 2p, Fe 2p, and O 1s. No other elements were detected within the detection limit. The C 1s peak (284.6 eV) was used as reference for the binding energy correction. XPS results clearly indicate the successful formation of ferrite phases after annealing.

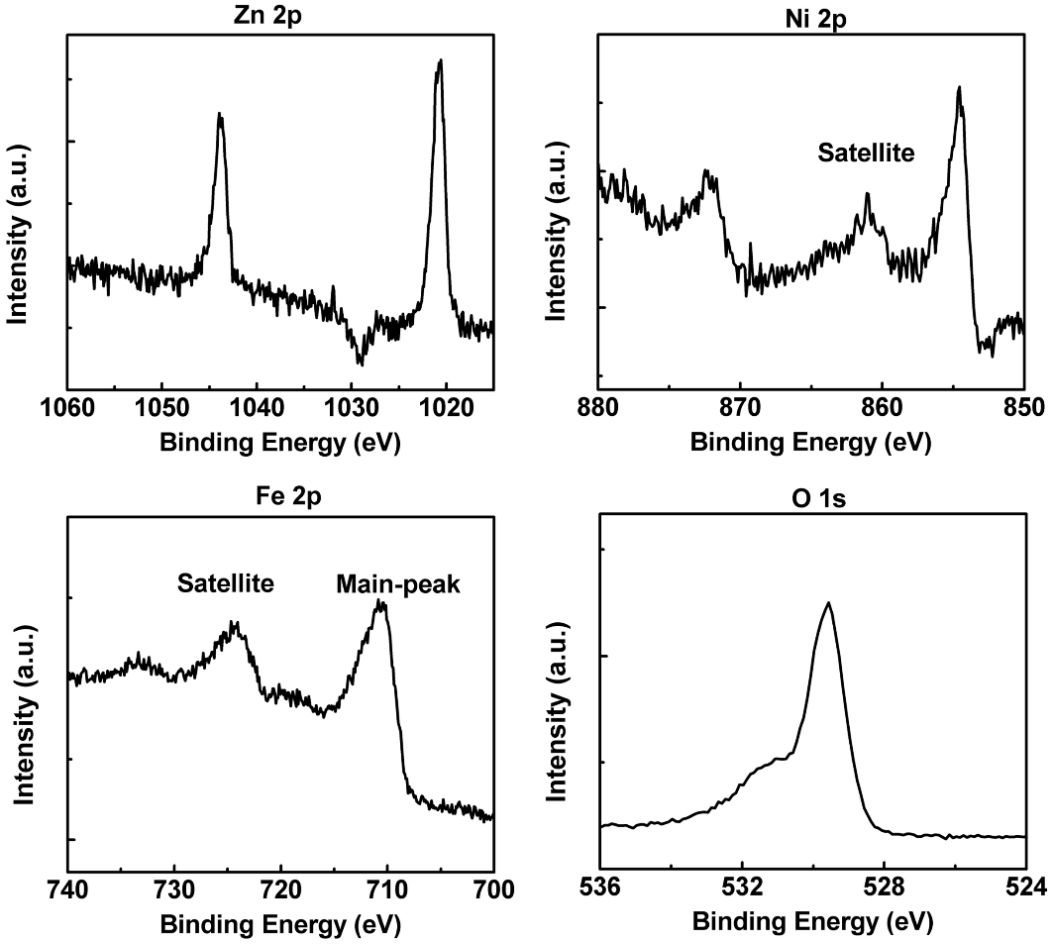

Figure S2 X-ray photoelectron spectra of printed magnetic filter after sintering at 1300 ^{o}C.

Synthesis of iron oxide nanoparticles

Fe_3O_4 nanoparticles were prepared by a well-established thermal decomposition method. Iron(III) acetylacetonate and oleic acid were added to benzyl ether, and magnetically stirred under a flow of nitrogen. The reaction mixture was slowly heated to 165 ^oC, then heated to reflux for 30 min. The particle size was adjusted by varying the heating temperature and reaction time. Subsequent, the ontained hydrophobic Fe_3O_4 nanoparticles were transferred to water via a ligand-exchange reaction whereby PAA displaced as a surfactant. The same procedure was used to modify different sized Fe_3O_4 nanoparticles. At the same time, FT-IR spectrum shown in Figure S3 was performed to verify the successful surface modification by PAA.

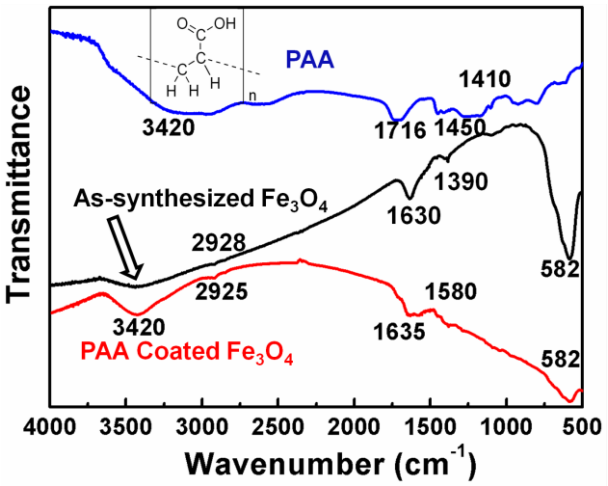

Figure S3 FT-IR spectrum of the PAA (Mw = 1800), as-synthesized Fe_3O_4 nanoparticles, and PAA-coated Fe_3O_4 nanocomposites.

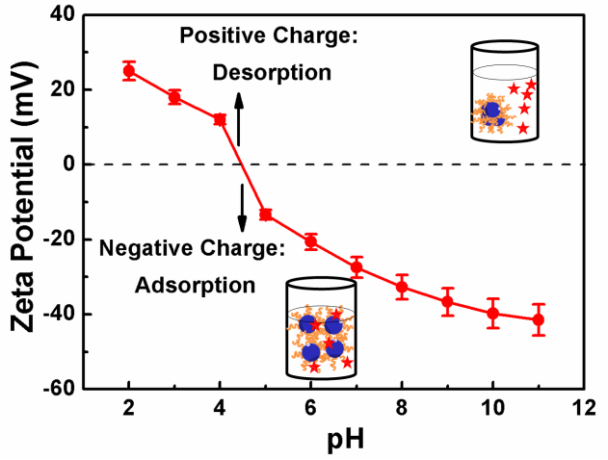

Figure S4 Zeta potential of PAA-coated Fe_3O_4 nanocomposites.

Adsorption behavior of iron oxide nanoparticles

The adsorption behaviors of Pb(II) on Fe_3O_4 nanocomposites were fitted by the pseudo-second-order kinetic model and Langmuir isotherm model with parameters summarized in Table S3.The maximum adsorption capacity was compared with other works in the literature (Table S4).

Table S3 Summary of PAA-coated Fe_3O_4 nanocomposites on Pb(II) adsorption behavior (pH 7.0).

Samples	Pb(II) adsorption					
	Pseudo-second-order kinetic model			Langmuir model		
	k (g mg^{-1} min^{-1})	q_e (mg g^{-1})	R^2	b (L mg^{-1})	q_m (mg g^{-1})	R^2
1	0.0037	107.52	0.999	0.025	454.55	0.998
2	0.0038	117.65	0.999	0.029	476.19	0.998

Table S4 Comparison of lead adsorption capacities.[1-7]

Adsorbents	Pb(II) concentration range (mg L^{-1})	q_m (mg g^{-1})	Reference
$MnFe_2O_4$-MoS_2–carbon dot	10-1000	588.24	1
$CoFe_2O_4$-MoS_2–carbon dot		660.67	
Acetoacetanilide-Fe_3O_4	50-400	392.2	2
GO-$MnFe_2O_4$ nanohybrids	1-400	673	3
Fe_3O_4@DAPF	10-100	83.3	4
α-Fe_2O_3 nanoboxes	40-1000	900	5
Fe_3O_4/Humic acid	0.01-5	97.7	6
Fe_3O_4/EDTA	1-100	102.2	7
Fe_3O_4/PAA	10-450	476	Our work

Effect of pH, temperature, and the amount of adsorbents

The effect of pH on heavy metal adsorption (e.g., Pb(II)) is presented in Figure S5a. As we can see, adsorption capacity increased with pH. However, the adsorption at pH above 7.0 decreased due to the formation of precipitation. Moreover, as illustrated in Figure S5b, the adsorption capacity gradually increased up to the optimum dosage (2 mg), beyond which the capacity did not change much due to a fixed number of adsorption sites. Temperature still had an influence on the adsorption as shown in Figure S5c. It was found that lead adsorption increased with increase in temperature resulted from the diffusion of the solution.

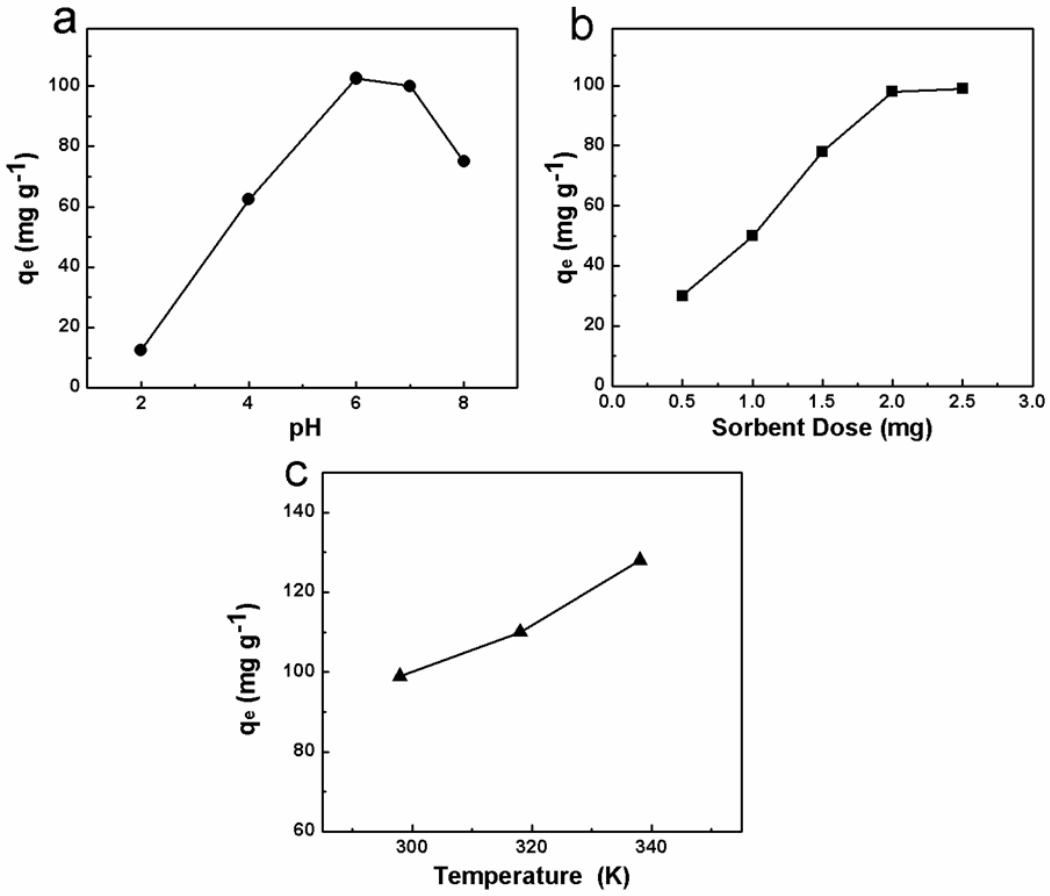

Figure S5 (a) Adsorption of Pb(II) ions on Fe_3O_4 nanocomposites at different pH values, with the initial concentration of 10 mg L^{-1}, and adsorbent dose of 2 mg. (b) Adsorption of Pb(II) ions on Fe_3O_4 nanocomposites in different amount from 0.5 mg to 3.0 mg, Pb(II) initial concentration was 10 mg L^{-1} at pH 7.0. (c) Adsorption of Pb(II) ions on Fe_3O_4 nanocomposites at 298, 318, 338 K, with the initial concentration of 10 mg L^{-1}, and adsorbent dose of 2 mg at pH 7.0.

Adsorption mechanism

As illustrated in Figure S6a, the FT-IR peak of carbonyl groups stretching at 1635 cm^{-1} shifts to 1570 cm^{-1} after adsorption, Pb(II) for example. Also, XPS spectra show two clear peaks at binding energy of 138.5 and 143.4 eV corresponding to Pb 4f after adsorption. Meanwhile, as the deconvoluted C1s spectrum shown in Figure S6c and d, the peaks of C-O-H and C=O bond after adsorption clearly shift to higher binding energy at 286.3 and 288.7 eV, respectively. The results further confirm that carbonyl groups are involved in the lead uptake, which are consistent with FT-IR analysis.

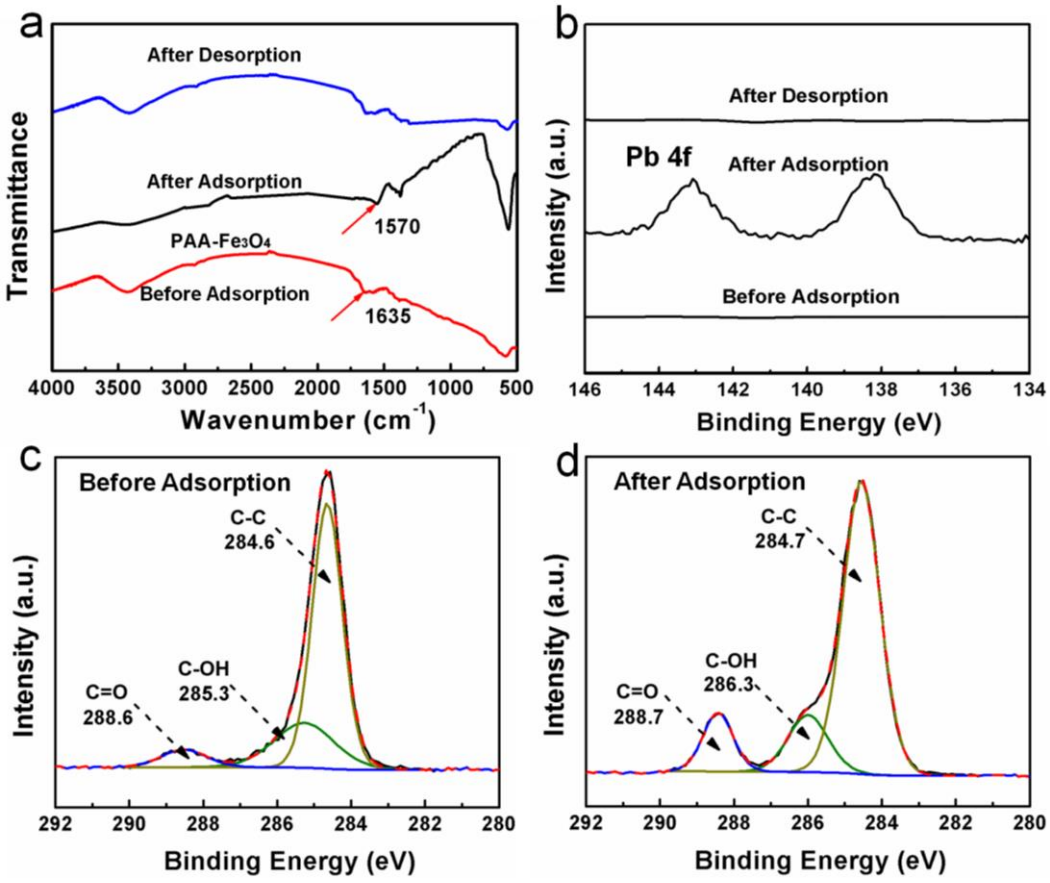

Figure S6 (a) FT-IR spectra of PAA-coated Fe_3O_4 nanoparticles before adsorption, after exposure to Pb(II) for 0.5 h, and after subsequent desorption in 0.1 M HCl. (b) XPS Pb 4f spectra of PAA-coated Fe_3O_4 nanoparticles before adsorption, after exposure to Pb(II) for 0.5 h, and after subsequent desorption in 0.1 M HCl. High resolution XPS spectra of PAA-coated Fe_3O_4 nanoparticles: C1s (c) before and (d) after Pb(II) adsorption.

The concentration of Fe_3O_4 nanoparticles in the filter

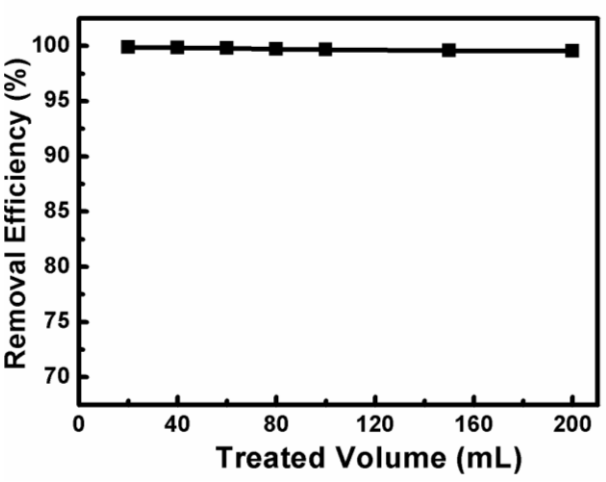

Figure S7 Removal efficiency of Fe_3O_4 nanoparticles (24 nm) with a high concentration of 500 mg L^{-1} when flowed through a single magnetic mesh with 20 layers.

Fabrication of nonmagnetic filter (α-Fe_2O_3) by 3D printing

The nonmagnetic filter was still shaped into 3D structures by extrusion 3D printing. Similarly, the as-prepared homogeneous paste was characterized by rheological behavior and thermogravimetric study as shown in Figure S8a and b. After post heat treatment, the measured magnetization by VSM (Figure S8c) was zero, indicating the nonmagnetic properties. Lastly, its phase was confirmed by the XRD analysis in Figure S8d.

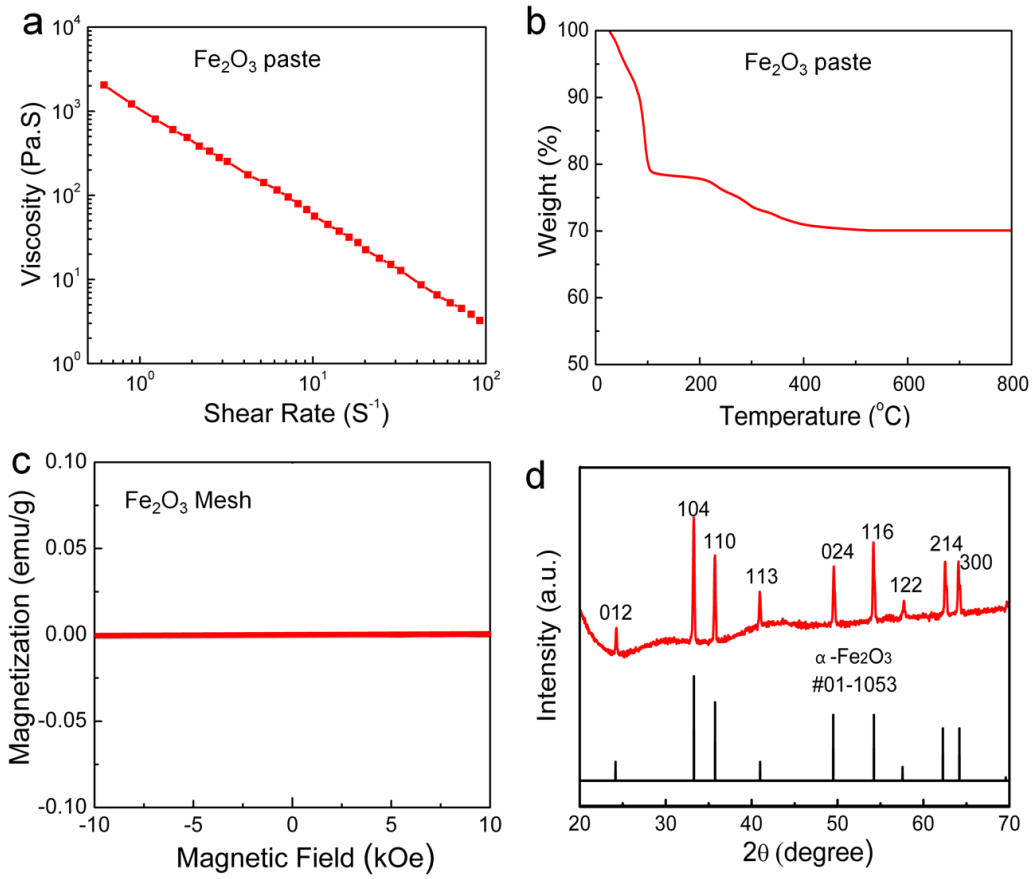

Figure S8 (a) Apparent viscosity as a function of shear rate of the prepared Fe_2O_3 paste for printing. (b) TGA results of the above paste heated at a ramp of 10 $^oC\ min^{-1}$ in nitrogen. (c) Magnetic hysteresis loops of the fabricated Fe_2O_3 mesh after heat treatment. (d) XRD patterns of the fabricated Fe_2O_3 mesh after heat treatment.

Reference:

(1) Wang, J.; Zhang, W.; Yue, X.; Yang, Q.; Liu, F.; Wang, Y.; Zhang, D.; Li, Z.; Wang, J. One-Pot Synthesis of Multifunctional Magnetic Ferrite–MoS_2–Carbon Dot Nanohybrid Adsorbent for Efficient Pb(Ⅱ) Removal. *J. Mater. Chem. A* **2016**, *4*, 3893-3900.

(2) Sharma, R. K.; Puri, A.; Monga, Y.; Adholeya, A. Acetoacetanilide-Functionalized Fe_3O_4 Nanoparticles for Selective and Cyclic Removal of Pb^{2+} Ions from Different Charged Wastewaters. *J. Mater. Chem. A* **2014**, *2*, 12888-12898.

(3) Kumar, S.; Nair, R. R.; Pillai, P. B.; Gupta, S. N.; Iyengar, M. A.; Sood, A. K. Graphene Oxide-$MnFe_2O_4$ Magnetic Nanohybrids for Efficient Removal of Lead and Arsenic from Water. *ACS Appl. Mater. Interfaces* **2014**, *6*, 17426-17436.

(4) Venkateswarlu, S.; Yoon, M., Core-Shell Ferromagnetic Nanorod Based on Amine Polymer Composite (Fe_3O_4@DAPF) for Fast Removal of Pb(II) from Aqueous Solutions. *ACS Appl. Mater. Interfaces* **2015**, *7*, 25362-25372.

(5) Mo, Q.; Wei, J.; Jiang, K.; Zhuang, Z.; Yu, Y. Hollow α-Fe_2O_3 Nanoboxes Derived from Metal–Organic Frameworks and Their Superior Ability for Fast Extraction and Magnetic Separation of Trace Pb^{2+}. *ACS Sustain. Chem. Eng.* **2016**, *5*, 1476-1484.

(6) Liu, J. F.; Zhao, Z. S.; Jiang, G. B. Coating Fe_3O_4 Magnetic Nanoparticles with Humic Acid for High Efficient Removal of Heavy Metals in Water. *Environ. Sci. Technol.* **2008**, *42*, 6949-6454.

(7) Huang, Y.; Keller, A. A. EDTA Functionalized Magnetic Nanoparticle Sorbents for Cadmium and Lead Contaminated Water Treatment. *Water. Res.* **2015**, *80*, 159-168.